Geophys. J. Int. (2009) **178,** 1614–1624 doi: 10.1111/j.1365-246X.2009.04253.x

An ambiguity in attenuation scattering imaging

W. A. Mulder[1,2] and B. Hak[2]

[1] *Shell International Exploration and Production,* PO Box 60, 2280 *AB, Rijswijk, The Netherlands. E-mail: wim.mulder@shell.com*
[2] *Department of Geotechnology, Faculty of Civil Engineering and Geosciences, Delft University of Technology,* PO Box 5048, 2600 *GA, Delft, The Netherlands*

Accepted 2009 May 14. Received 2009 May 13; in original form 2008 December 24

SUMMARY

Migration constructs a subsurface image by mapping band-limited seismic data to reflectors in the Earth, given a background velocity model that describes the kinematics of the seismic waves. Classically, the reflectors correspond to impedance perturbations on length scales of the order of the seismic wavelength. The Born approximation of the visco-acoustic wave equation enables the computation of synthetic data for such a model. Migration then amounts to solving the linear inverse problem for perturbations in density, velocity, and attenuation.

Here, the problem is simplified by assuming the density to be constant, leaving only velocity and attenuation perturbations. In the frequency domain, a single complex-valued model parameter that depends on subsurface position describes both. Its real part is related to the classic reflectivity, its imaginary part also involves attenuation variations. Attenuation scattering is usually ignored but, when included in the migration, might provide information about, for instance, the presence of fluids. We found, however, that it is very difficult to solve simultaneously for both velocity and attenuation perturbations. The problem already occurs when computing synthetic data in the Born approximation for a given scattering model: after applying a weighted Hilbert transform in the depth coordinate to a given scattering model, we obtained almost the same synthetic data if the scatterers had small dip and were located at not-too-shallow depths. This implies that it will be nearly impossible to simultaneously determine the real and imaginary part of the scattering parameters by linearized inversion without imposing additional constraints.

Key words: Inverse theory; Seismic attenuation; Wave scattering and diffraction.

1 INTRODUCTION

The oil and gas industry acquires seismic data to obtain an image of the subsurface that may reveal hydrocarbon bearing formations. Because a 3-D full visco-elastic inversion is computationally still out of reach, various approximations of the wave equation are employed, often based on ray tracing or one-way wave equations. These are often sufficiently accurate to obtain a structural image. A precise characterization of the subsurface that allows for volumetric estimates of the amounts of hydrocarbons in place requires a more accurate description. Visco-acoustic or visco-elastic full waveform inversion is computationally tractable in a 2-D approximation. However, the presence of local minima in the least-squares misfit functional makes the solution of the inverse problem difficult. One cause for this problem is the absence of low frequencies, below 8–10 Hz, in the seismic data.

The inverse problem becomes considerably simpler when linearized. Classic methods for velocity analysis provide a background velocity model. An operation called migration maps the band-limited seismic data to reflectors in the subsurface. Mathematically, this method amounts to a single iteration of a gradient based minimization of the least-squares misfit functional between observed and modelled data, using the Born approximation of the wave equation. Because this approximation assumes single scattering, the direct arrival and multiple reflections should be removed from the data before migration.

Examples (Østmo *et al.* 2002; Mulder & Plessix 2004) show that with proper weighting or preconditioning (Plessix & Mulder 2004), one or a few iterations with the conjugate-gradient method suffice to obtain a solution to the inverse problem when using the Born approximation of the constant-density visco-acoustic wave equation. The method works in the frequency-domain and reconstructs scatterers that represent perturbations of the background velocity model. In the frequency-domain, these are represented by complex numbers. The real part is almost entirely related to impedance perturbations, usually caused by abrupt changes in rock properties. If we include the imaginary part, we can formally obtain both velocity and attenuation perturbations. The latter, however, appeared to have no relation to physically realistic values in our numerical experiments.

To better understand why it may be difficult to reconstruct the imaginary part of the scattering perturbations, we consider the simple case of a 1-D model consisting of horizontally layered scatterers in a homogeneous background for the constant-density

visco-acoustic equation in Section 2. The scatterers correspond to perturbations both in velocity and attenuation. In Section 3, we derive the scattered wave field in the high-frequency case by means of the method of stationary phase. It turns out that there is an ambiguity that already occurs at the forward-modelling level: if we apply a weighted Hilbert transform in the depth coordinate to the scatterers, we obtain almost the same reflection data as for the original scatterers. As a consequence, least-squares fitting of observed data will lead to an inverse problem that is close to singular. We show that the 'true-amplitude' migration of the data, which amounts to the first iteration of a preconditioned conjugate-gradient minimization of the least-squares error, produces a reconstruction of the perturbations that is the average of the original and the transformed scattering model and has a minimum-norm property.

In Section 4, we address the question to what extent these conclusions carry over to a complex velocity model and dipping reflectors. We perform 2-D finite-difference simulations with a frequency-domain code that solves the system of equations that represents the Born approximation of the constant-density visco-acoustic wave equation.

We discuss the results in Section 5 and summarize the main conclusion in Section 6.

2 GOVERNING EQUATIONS

Migration maps seismic data recorded at the Earth's surface into an image of the subsurface. The implicit assumption is that the data only contain primaries and that surface or interbed multiples are absent or negligible. We can generate such data using the Born approximation of the wave equation. In this approximation, the subsurface model is split into a part that does not produces significant reflections in the seismic frequency band and perturbations that generate the reflection data. For the acoustic wave equation, reflections can be avoided by defining the density in such a way that the impedance is constant. For constant-density acoustics, we use a smooth background velocity. The perturbations are then obtained as the difference between the original rough velocity model and its smoothed version that serves as the background model.

In the frequency domain, the constant-density visco-acoustic wave equation is

$$-\frac{\omega^2}{v^2}\hat{p} - \Delta\hat{p} = s. \tag{1}$$

Here $\hat{p}(\omega, \mathbf{x})$ is the pressure, $\omega = 2\pi f$ with f the frequency, $s(\omega, \mathbf{x})$ is a source term and the complex velocity $v(\omega, \mathbf{x})$ is given by (*cf.* Aki & Richards 1980, eq. 5.88)

$$\frac{1}{v} = \frac{1}{c}\left[1 - \frac{1}{\pi Q}\log(f/f_{\rm r}) + \frac{\rm i}{2Q}\right],$$

with real-valued velocity $c(\mathbf{x})$ and quality factor $Q(\mathbf{x})$. The latter is usually much larger than 1. Causality requires the logarithmic term with reference frequency $f_{\rm r}$.

By linearizing eq. (1) with respect to the model, we obtain the Born approximation

$$-\omega^2 v_0\hat{p}_0 - \Delta\hat{p}_0 = s, \quad -\omega^2 v_0\hat{p}_1 - \Delta\hat{p}_1 = \omega^2 v_1\hat{p}_0, \tag{2}$$

with model parameters $v = v^{-2} = v_0 + v_1$, where $v_0(\omega, \mathbf{x}) = v_0^{-2}$ represents a smooth background velocity model v_0 that should not produce significant scattering in the seismic frequency band and $v_1(\omega, \mathbf{x}) = v^{-2} - v_0^{-2}$ a perturbation term that is responsible for the scattering of incoming waves. For simplicity, we will assume that $v_1(\omega, \mathbf{x}) = v_1(\mathbf{x})$, independent of ω.

For the Fourier transform in time, we adopt the convention $p(\mathbf{x}, t) = (2\pi)^{-1}\int_{-\infty}^{\infty}\hat{p}(\omega, \mathbf{x})e^{-i\omega t}\,d\omega$. We will denote the Hilbert transform of a function $g(z)$, depending on z, by $\mathcal{H}_z[g]$. This amounts to convolution with $(\pi z)^{-1}$ in the depth domain.

3 3-D HOMOGENEOUS BACKGROUND WITH 1-D SCATTERING MODEL

3.1 Scattered wavefield

We make the following simplifying assumptions. The background velocity model is defined by the constants c_0 and Q_0, whereas the perturbation $v_1(z)$ only depends on depth. The source is a delta function located at $x_s = -h < 0$, $y_s = 0$, $z_s = 0$, and we consider a single receiver at $x_r = +h$, $y_r = 0$, $z_r = 0$. We assume that ω is finite but large enough to justify the application of the method of stationary phase.

The background pressure is given by the 3-D Green's function

$$\hat{p}_0(\omega, \mathbf{x}) = \frac{e^{ik_0 r_s}}{4\pi r_s}, \quad k_0 = \frac{\omega}{v_0}, \quad r_s = \sqrt{(x+h)^2 + y^2 + z^2}.$$

Note that k_0 is complex because v_0 is. The scattered field at the receiver is

$$\hat{p}_1(\omega, h) = \int_{-\infty}^{\infty}dx\int_{-\infty}^{\infty}dy\int_0^{\infty}dz\,\frac{\omega^2 e^{ik_0(r_s+r_r)}}{16\pi^2 r_s r_r}v_1(z), \tag{3}$$

with $r_r = \sqrt{(x-h)^2 + y^2 + z^2}$. We assume that scattering only occurs beyond a depth $z_m > 0$, so $v_1(z) = 0$ for $z \le z_m$.

Integration over x and y of eq. (3) with the method of stationary phase leads to

$$\hat{p}_1(\omega, h) \simeq \frac{i\omega c_0}{16\pi}\int_0^{\infty}dz\,f_1(z)\mu(z), \tag{4}$$

with

$$f_1(z) = e^{2ik_0\sqrt{z^2+h^2}}, \quad \mu(z) = \frac{v_1(z)}{z}.$$

3.2 Ambiguity

While inspecting migration images obtained with a 2-D constant-density visco-acoustic finite-difference code, we noted that the real and imaginary parts resembled each other's Hilbert transform. This suggested that demigration, which amounts to forward modelling of the scattering model obtained by migration, would yield data that should closely resemble the original data. This indeed turned out to be the case and led to the conclusion that a given scattering model and its Hilbert transform, with suitable weighting and scaling, would produce the same data. For the simplified model problem considered in this section, this means that $\int_{-\infty}^{\infty}dz\,f_1\mu$ should be the same as $-i\int_{-\infty}^{\infty}dz\,f_1\mathcal{H}_z[\mu]$. Because $\int_{-\infty}^{\infty}dz\,f_1\mathcal{H}_z[\mu] = -\int_{-\infty}^{\infty}dz\,\mu\mathcal{H}_z[f_1]$, we can proceed without $\mu(z)$ and concentrate on $\mathcal{H}_z[f_1]$. If we could prove that $i\mathcal{H}_z[f_1] = f_1$, then we would have demonstrated that μ and $-i\mathcal{H}_z[\mu]$ would lead to the same data for arbitrary $\mu(z)$, so for any scattering model. It will turn out that $i\mathcal{H}_z[f_1]$ and f_1 are different, but that the difference may be small.

To evaluate the integral $I_1 = \mathcal{H}_z[f_1]$, we consider the closed contour C sketched in Fig. 1, which can be interpreted as two closed contours glued together, one in the first quadrant of the complex plane and one in the third. The integral

$$I(z) = \frac{1}{\pi}\int_C\frac{f_1(\zeta)}{z-\zeta}d\zeta = 0.$$

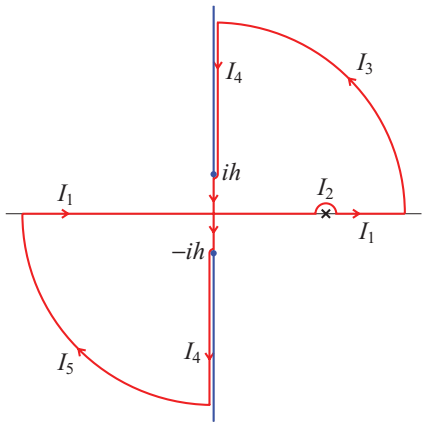

Figure 1. Two closed contours are glued together to evaluate $\mathcal{H}_z[f_1]$. The blue lines mark the branch-cuts of $\sqrt{h^2+\zeta^2}$. The cross indicates the pole.

Now $I = I_1 + I_2 + I_3 + I_4 + I_5$, with $I_1 = \mathcal{H}_z[f_1]$, I_2 the contribution at the pole $\zeta = z$, I_3 the result for the arc in the first quadrant when its radius goes to infinity, I_4 the integral over the imaginary axis downward, where we have to stay on the proper side of the branch-cut of $\sqrt{h^2+\zeta^2}$, and I_5 the result for the arc in the third quadrant. The residual theorem yields $I_2 = \mathrm{i} f_1(z)$ at the pole if $z > 0$. For $z < 0$, we have to traverse the pole, which now lies on the negative real axis, from below, resulting in $I_2 = -\mathrm{i} f_1(z)$. Therefore, $I_2(z) = \mathrm{i} f_1(z)\,\mathrm{sign}(z)$. The arcs provide $I_3 = 0$ and $I_5 = 0$. The integral over the imaginary axis leads to

$$I_4 = -\frac{1}{\pi}\int_{-\infty}^{\infty} \mathrm{d}(\mathrm{i}\tilde{\eta})\,\frac{\mathrm{e}^{2\mathrm{i}k_0\sqrt{h^2-\tilde{\eta}^2}}}{z-\mathrm{i}\tilde{\eta}} = -\mathrm{i}[f_2(z)+f_3(z)],$$

with

$$f_2(z) = \frac{2\tilde{z}}{\pi}\int_0^1 \mathrm{d}\eta\,\frac{\mathrm{e}^{\mathrm{i}\alpha\sqrt{1-\eta^2}}}{\tilde{z}^2+\eta^2}, \qquad f_3(z) = \frac{2\tilde{z}}{\pi}\int_1^{\infty} \mathrm{d}\eta\,\frac{\mathrm{e}^{-\alpha\sqrt{\eta^2-1}}}{\tilde{z}^2+\eta^2}.$$

Here $\tilde{z} = z/h$ and $\alpha = 2k_0h$ with $\alpha_\mathrm{r} = \mathrm{Re}\,\alpha > 0$ and $\alpha_\mathrm{i} = \mathrm{Im}\,\alpha > 0$. As a result,

$$f_4(z) = \mathrm{i}\,\mathrm{sign}(z)\mathcal{H}_z[f_1] = f_1 + (f_2+f_3)\,\mathrm{sign}(z). \tag{5}$$

We have now found that $\mathrm{i}\mathcal{H}_z[f_1]$ and f_1 are different. Apart from the extra factor, sign(z), which is just a technicality if $\mu(z) = 0$ for $z \le 0$, there is a remainder $(f_2 + f_3)\,\mathrm{sign}\,(z)$. If we could show that both $|f_2|$ and $|f_3|$ are significantly smaller than $|f_1|$, we would have the relation $\mathrm{i}\,\mathrm{sign}(z)\mathcal{H}_z[f_1] \simeq f_1$. Then, the recorded pressure is proportional to

$$\int_{-\infty}^{\infty} \mathrm{d}z\; f_1(z)\mu(z) \simeq -\mathrm{i}\int_{-\infty}^{\infty} \mathrm{d}z\; f_1(z)\mathcal{H}_z[\mu(z)\,\mathrm{sign}(z)],$$

which implies that almost the same data will be observed for $\nu_1(z)$ and $\tilde{\nu}_1(z) = -\mathrm{i}|z|\mathcal{H}_z[\nu_1(z)/z]$.

Before considering the remainder $(f_2 + f_3)\,\mathrm{sign}\,(z)$, we will use eq. (5) to refine the definition of the depth-weighted, scaled Hilbert transform. We assumed earlier that $\nu_1(z) = 0$ for negative z. The transformed model $\tilde{\nu}_1(z)$, however, may have non-zero values for negative z. Because $f_1(z)$ is symmetric in z, we can take $\tilde{\nu}_1(z)$ for $z < 0$, mirror it with respect to $z = 0$, and add it to the transformed model at positive z. This can be summarized by defining the depth-weighted, scaled Hilbert transform of a function $g(z)$ as

$$\mathcal{M}[g](z) = \tilde{g}(z) + \tilde{g}(-z), \qquad \tilde{g}(z) = -\mathrm{i}|z|\mathcal{H}_z[g/z],$$

where $z \ge 0$, and we assume that $g(z) = 0$ for $z \le 0$.

It still remains to be shown under which conditions the term in eq. (5) with f_2 and f_3 is small relative to f_1. We list some bounds that may help to evaluate for which parameters of the background model and for which depths, given by $\tilde{z} = z/h$, f_2 and f_3 are much smaller than f_1. We have

$$|f_1| = \mathrm{e}^{-\alpha_\mathrm{i}\sqrt{1+\tilde{z}^2}},$$

and, assuming $\tilde{z} \ge 0$,

$$|f_2| \le \frac{2\tilde{z}}{\pi}\int_0^1 \mathrm{d}\eta\,\frac{1}{\tilde{z}^2+\eta^2} = \frac{2}{\pi}\arctan(1/\tilde{z}),$$

whereas

$$|f_3| \le \frac{2\tilde{z}}{\pi}\int_1^{\infty} \mathrm{d}\eta\,\frac{\mathrm{e}^{-\alpha_\mathrm{r}(\eta-1)}}{1+\eta^2} = \frac{2}{\pi\alpha_\mathrm{r}}\frac{\tilde{z}}{1+\tilde{z}^2}.$$

The bounds for $|f_2|$ and $|f_3|$ are not very sharp.

To understand the bound on f_1, recall that $\alpha = 2k_0h = \alpha_\mathrm{r} + \mathrm{i}\alpha_\mathrm{i}$. If the damping of the background model is small, then $\alpha_\mathrm{i} \ll \alpha_\mathrm{r}$ and $\mathrm{Re}\,k_0 \simeq \omega/c_0$. The bound for f_1 merely states that the data amplitudes for larger depths will decrease due to damping. Note that the amplitude decay due to the geometrical spreading is contained in the factor $1/z$ that was absorbed in the definition of μ. If $|f_1|$ becomes significantly smaller than 1, then the data will not be useful in practice when noise is present.

The bound on f_3 contains α_r, which generally is much larger than 1—otherwise the method of stationary phase would not be applicable. As a result, the bound on $|f_3|$ is much smaller than the bound on $|f_2|$.

At this point, it still is not clear whether or not the term with $f_2 + f_3$ in eq. (5) is much smaller than f_1; so, we will continue with a numerical example.

3.3 Example

We choose a background velocity $c_0 = 1500\,\mathrm{m\,s^{-1}}$, a quality factor $Q_0 = 100$, a frequency $f = 15\,\mathrm{Hz}$ and a reference frequency $f_\mathrm{r} = 1\,\mathrm{Hz}$. These are typical values for a marine seismic survey. Fig. 2 plots the moduli of f_1, f_2 and f_3 as a function of z/h for half-offsets h of 50 and 1000 m. We observe that f_1 is much larger than f_2 and f_3 over a range of depths. The contribution of f_3 can be neglected. At larger depths, the graph of $|f_1|$ drops because of the damping in the background medium. By the time it reaches f_2, the signal may have become too weak to be useful in practice, in the presence of noise, multiples and so on. At the other end, where depth is small relative to offset, we can no longer neglect f_2. For a large range of depths, however, the term $f_2 + f_3$ in eq. (5) will be small relative to f_1.

Even if $f_2 + f_3$ is small compared with f_1, $P_2 = \int_{-\infty}^{\infty} \mathrm{d}z\,[f_2(z)+f_3(z)]\,\mathrm{sign}(z)\,\mu(z)$ does not have to be small relative to $P_1 = \int_{-\infty}^{\infty} \mathrm{d}z\; f_1(z)\mu(z)$. Figs 3 and 4 show that $f_1(z)$ is oscillatory, whereas f_2 is smooth and f_3 negligible. If $\mu(z)$ represents an isolated reflector localized at not too small a depth, with a thickness of the order of the wavelength of the dominant signal or less, we can expect P_2 to be smaller than P_1. If, however, μ varies slowly over many oscillations of f_1, the net result may be that P_1 becomes of the same size or smaller than P_2.

We will first give a numerical example and then study the spatial Fourier transform in depth to obtain more insight into which models $\mu(z)$ will provide similar data after a weighted Hilbert transform. Fig. 5 shows a scattering model with a number of isolated reflectors and its transform. The recorded pressure data are displayed in Fig. 6,

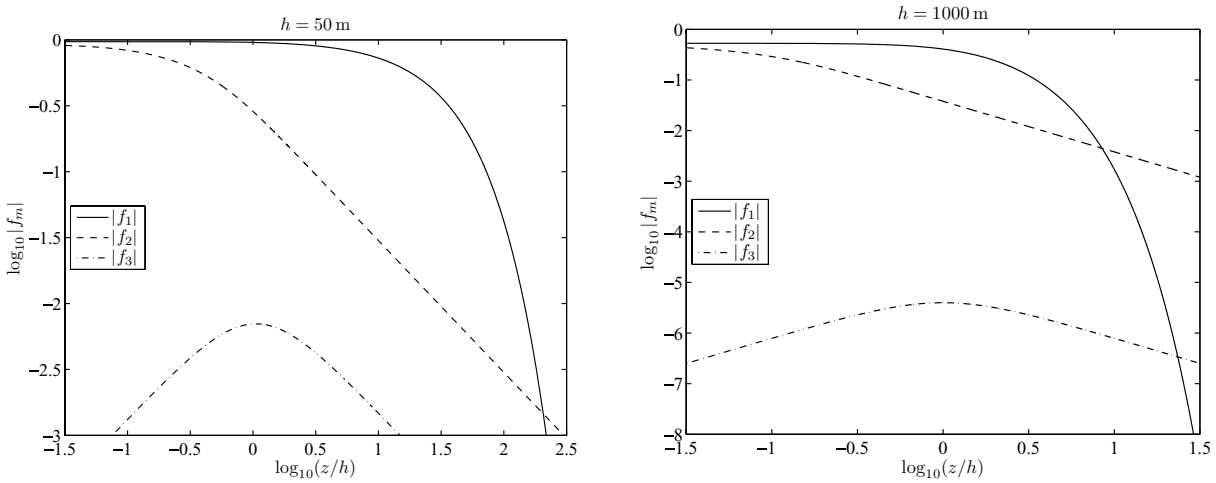

Figure 2. Moduli of f_1, f_2, f_3 at half-offsets of 50 and 1000 m, showing that f_1 dominates f_2 and f_3 over a substantial range of depths. Note the difference in range for the vertical axis between the two cases.

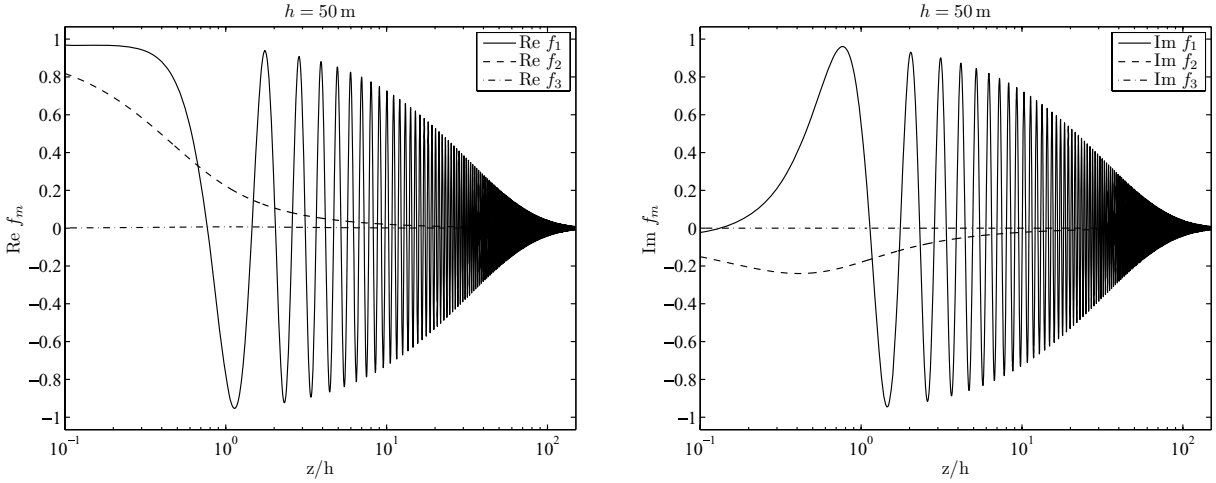

Figure 3. Real (left-hand panel) and imaginary (right-hand panel) part of f_1, f_2, f_3 at a half-offset of 50 m, showing that f_1 dominates f_2 and f_3 over a substantial range of depths but is also far more oscillatory. Note the logarithmic scale for z/h.

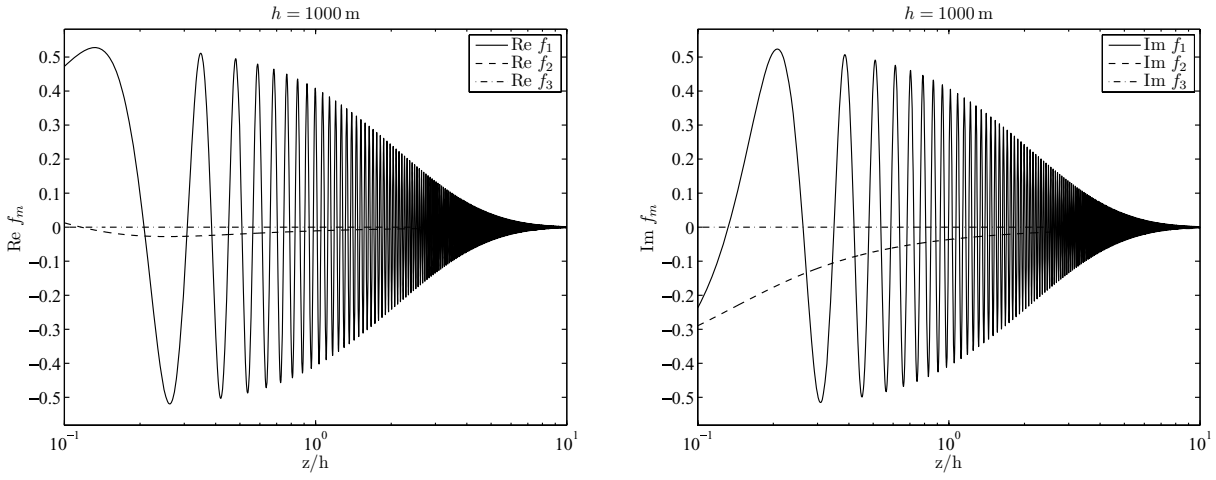

Figure 4. As Fig. 3, but for a half-offset of 1000 m.

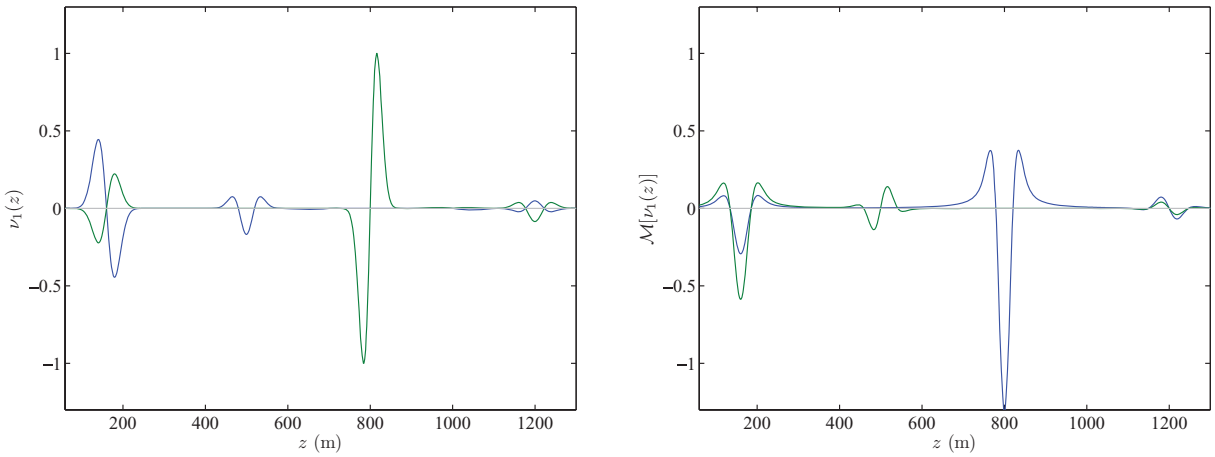

Figure 5. The left-hand panel shows the scatterer model $\nu_1(z)$. The blue line represents the real part of the squared slowness perturbation, the green line its imaginary part. The right-hand panel displays $\mathcal{M}[\nu_1]$, its scaled, depth-weighted Hilbert transform.

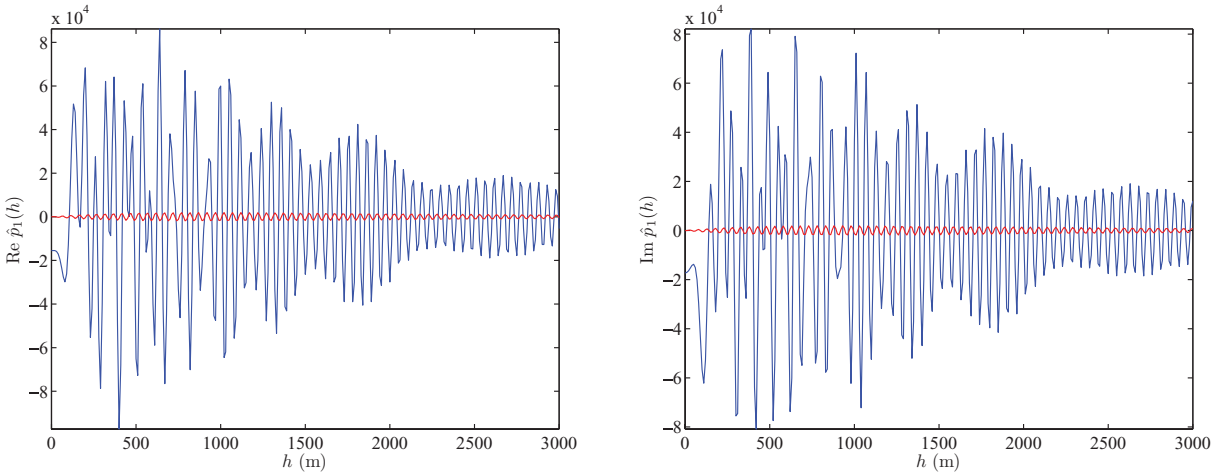

Figure 6. Real part (left-hand panel) and imaginary part (right-hand panel) of the recorded pressure, in arbitrary units, as a function of the half-offset h. The blue line represents the pressure for the original model, the red one the difference between the data for the transformed and original model.

together with the difference between the data for the transformed and original model. The differences are an order of magnitude smaller than the data for the entire range of half-offsets. We found a similar behaviour for smaller and larger frequencies within the typical seismic frequency band of 8–80 Hz or so. This clearly illustrates that two different models, related by a scaled, depth-weighted Hilbert transform, provide nearly identical data.

Note that the data difference between the two models could have been computed directly by taking a scattering model $\nu_1 - \mathcal{M}[\nu_1]$. This implies that a given scattering model $\nu_1(z)$ can be 'cloaked' by replacing it with $\nu_1 - \mathcal{M}[\nu_1]$, shown in Fig. 7 for the current example.

3.4 Fourier representation

To learn more about which scattering models provide more or less the same data before and after a weighted Hilbert transform, we consider the Fourier transform in depth.

The spatial Fourier transform $\hat{\mu}(\kappa)$ as a function of wavenumber κ is defined in such a way that $\mu(z) = (2\pi)^{-1}\int_{-\infty}^{\infty} d\kappa\, \hat{\mu}(\kappa)\mathrm{e}^{\mathrm{i}\kappa z}$. Note that the use of the hat in the notation is potentially confusing, as we used it earlier for the temporal Fourier transform. We can write

$$\int_{-\infty}^{\infty} \mathrm{d}z\, f_1(z)\mu(z) = \int_{-\infty}^{\infty} \mathrm{d}\kappa\, \hat{\mu}(\kappa)G(\kappa),$$

where

$$G(\kappa) = \frac{1}{2\pi}\int_{-\infty}^{\infty} \mathrm{d}z\, f_1(z)\mathrm{e}^{\mathrm{i}\kappa z} = -hk_0 H_1^{(1)}(h\eta)/\eta, \tag{6}$$

with $\eta = \sqrt{4k_0^2 - \kappa^2}$. This is a generalization of eq. (3.914) in Gradshteyn & Ryzhik (1965). Here $H_1^{(1)}(\zeta)$ is a Hankel function of the first kind. Note that $G(\kappa) = G(-\kappa)$ for real κ. Also, $\hat{f}_1(\kappa) = 2\pi G(\kappa)$. Recall that $\mathrm{Re}\, k_0 > 0$ and $\mathrm{Im}\, k_0 > 0$.

In the Fourier domain, the Hilbert transform amounts to multiplication by $-\,\mathrm{i}\,\mathrm{sign}\,(\kappa)$. The Fourier transform of $f_4(z) = \mathrm{i}\,\mathrm{sign}(z)\mathcal{H}_z[f_1]$ is

$$\hat{f}_4(\kappa) = -\mathrm{i}\mathcal{H}_\kappa[\hat{f}_1(\kappa)\,\mathrm{sign}(\kappa)].$$

Because we have assumed that $\mu(z) = 0$ for $z < z_m$, with $z_m > 0$, we should have $\mu(z) = H(z)\mu(z)$, where $H(z)$ is the Heaviside or unit step function. This results in $\hat{\mu} = -\mathrm{i}\mathcal{H}_\kappa[\hat{\mu}]$ and

$$\int_{-\infty}^{\infty} \mathrm{d}\kappa\, \hat{f}_4(\kappa)\hat{\mu}(\kappa) = \int_{-\infty}^{\infty} \mathrm{d}\kappa\, \hat{f}_1(\kappa)\hat{\mu}(\kappa)\,\mathrm{sign}(-\kappa).$$

If $f_4(z) \simeq f_1(z)$, we find that

$$\int_{-\infty}^{\infty} \mathrm{d}\kappa\, \hat{f}_1(\kappa)\hat{\mu}(\kappa)\,\mathrm{sign}(-\kappa) \simeq \int_{-\infty}^{\infty} \mathrm{d}\kappa\, \hat{f}_1(\kappa)\hat{\mu}(\kappa). \tag{7}$$

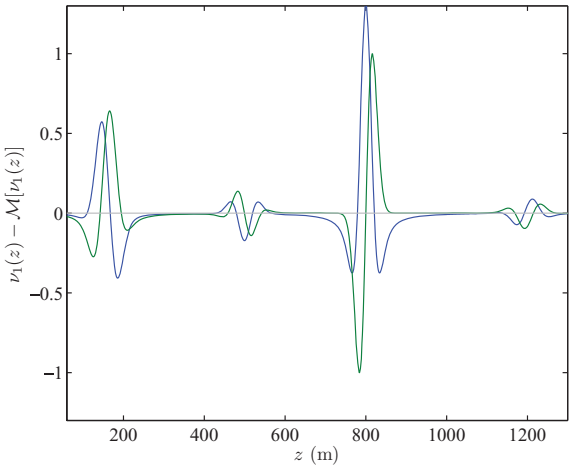

Figure 7. Model that directly produces the data difference in Fig. 6 and therefore can be considered a cloaked version of the original model in Fig. 5. The blue line corresponds to the real part and the green to the imaginary part of $\nu_1 - \mathcal{M}[\nu_1]$.

This means that the recorded pressure hardly depends on the positive wavenumbers of $\hat{\mu}(\kappa)$.

As an illustration, Fig. 8 displays the Fourier transforms of f_1 and f_4 for a half-offset of 50 m. The other parameters are the same as before. The real part has large peaks at $\kappa = \pm \mathrm{Re}\, 2k_0$, which is the wavelength of the scattering model to which the wavefield is most sensitive. The functions $\hat{f}_1(\kappa)$ and $\hat{f}_4(\kappa)$ agree quite well except for small κ, where a singularity in $\hat{f}_4(\kappa)$ appears. Fig. 9 shows the same functions at a half-offset of 1000 m. The singularity at $\kappa = 0$ is prominent. At this larger offset, the wavefield is sensitive to a wider range of wavelengths, involving the less oscillatory components of the scattering model. This fact was exploited by Sirgue & Pratt (2004) to reduce the number of frequencies required to obtain sufficient wavelength coverage in frequency-domain full waveform inversion.

From these figures, we learn that the effect on the recorded data of the difference between $\hat{f}_1(\kappa)$ and $\hat{f}_4(\kappa)$ will be small if $\hat{\mu}(\kappa)$, the Fourier transform of the scattering model, does not contain small wavenumbers. This means that $\mu(z)$, or $\nu_1(z)$, should be sufficiently oscillatory as a function of depth. Since $\mu(z)$ was defined as the depth-weighted difference between a rough earth model and its smoothed version, it will be oscillatory by construction. As seismic data are band-limited, linearized inversion or migration will only construct the oscillatory components of the scatterers—the boundaries between different types of rock. In that case, the ambiguity will show up. We will consider this next.

3.5 Migration

Given measured data, we can reconstruct the reflectivity $\nu_1(z)$ by solving the inverse problem. In geophysics, this operation is called migration. Migration is usually implemented as a single iteration step for a gradient-based minimization method with a suitable weighting or preconditioning, based on the diagonal of the Hessian of the inverse problem (Beylkin 1985; Docherty 1991; ten Kroode *et al.* 1994; Gray 1997; Chavent & Plessix 1999; Shin *et al.* 2001; Plessix & Mulder 2004).

Consider the least-squares error $J = \frac{1}{2}\sum_{h,\omega} |\hat{p}_1(\omega, h) - \hat{p}_1^{\mathrm{obs}}(\omega, h)|^2$, where $\hat{p}_1 = F\nu_1$ are modelled data and $\hat{p}_1^{\mathrm{obs}}$ observed data for receivers located at a finite number N_h of offsets. The linear operator F is defined by eq. (4). The inverse problem requires the solution of $F^{\mathrm{H}} F \nu_1 = F^{\mathrm{H}} \hat{p}_1^{\mathrm{obs}}$. Here F^{H} denotes the conjugate transpose. The Hessian $F^{\mathrm{H}}\ F$ is singular or close to singular, as follows from the previous section.

The weighted migration result is

$$m(z_1) \propto \sum_{\omega,h} \omega^2 \int_{z_m}^{\infty} \mathrm{d}z_2\, \frac{|z_1|}{z_2} \mathrm{e}^{2\mathrm{i}(k_0 r_2 - k_0^* r_1)} \nu_1(z_2).$$

Here $r_k = \sqrt{z_k^2 + h^2}$ for $k = 1, 2$. The asterisk denotes the complex conjugate. The weighted Hilbert transform, $\mathcal{H}_z[m/|z_1|]$, involves $\mathcal{H}_z[f_1^*]$. Therefore, $\mathcal{H}_z[m/|z_1|] \simeq \mathrm{i}(m/|z_1|)$. This shows that $m/|z_1|$ has a minimum-norm property in the following sense.

Among all linear combinations $(1 - w)\mu - wi\mathcal{H}[\mu]$ with complex w, the one with $w = \frac{1}{2}$ has the smallest norm. To prove this, we start with the norm of a complex-valued function $a(z)$: $||a|| = [\int_{-\infty}^{\infty} |a|^2 \mathrm{d}z]^{1/2}$. The Hilbert transform of $a(z)$ is abbreviated as $\breve{a} = \mathcal{H}[a]$, and we set $b = -\mathrm{i}\breve{a}$. Then $b_{\mathrm{r}} = \mathrm{Re}\, b = \breve{a}_{\mathrm{i}} = \mathrm{Im}\, \breve{a}$ and $b_{\mathrm{i}} = \mathrm{Im}\, b = -\breve{a}_{\mathrm{r}} = -\mathrm{Re}\, \breve{a}$. The Hilbert transform has the property that $||a_{\mathrm{r}}|| = ||\breve{a}_{\mathrm{r}}||$ and $||a_{\mathrm{i}}|| = ||\breve{a}_{\mathrm{i}}||$. Also, $\int_{-\infty}^{\infty} a_{\mathrm{r}} b_{\mathrm{i}} \mathrm{d}z = -\int_{-\infty}^{\infty} a_{\mathrm{r}} \breve{a}_{\mathrm{r}}\, \mathrm{d}z = 0$ and $\int_{-\infty}^{\infty} a_{\mathrm{i}} b_{\mathrm{r}} \mathrm{d}z = \int_{-\infty}^{\infty} a_{\mathrm{i}} \breve{a}_{\mathrm{i}}\, \mathrm{d}z = 0$. Let

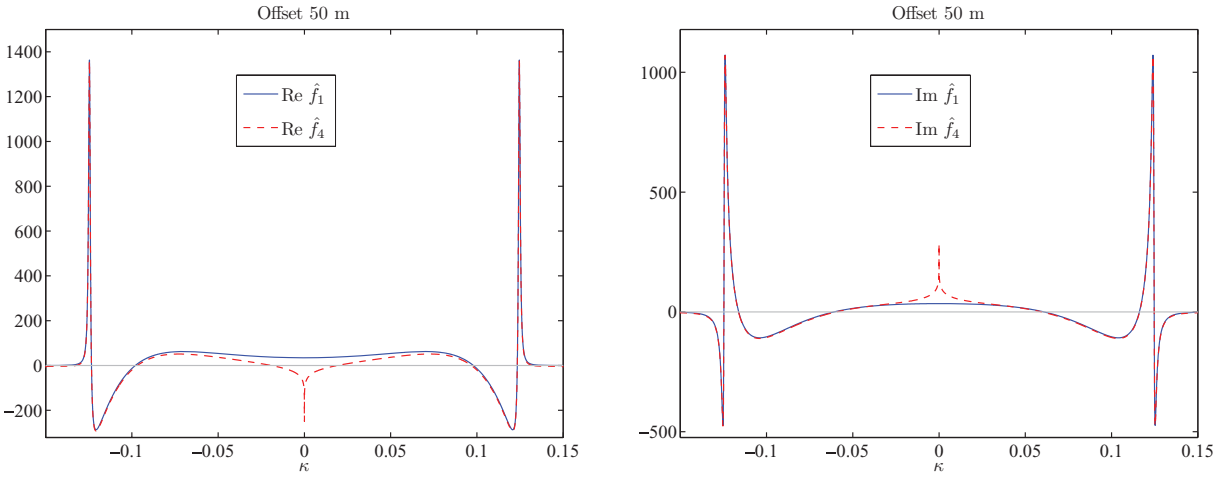

Figure 8. Fourier transforms of $f_1(z)$, the kernel between the scattering model and the recorded pressure, and $f_4(z)$, its weighted Hilbert transform, at a half-offset of 50 m. The left-hand panel shows the real part of these functions, the right-hand panel the imaginary part. The functions $\hat{f}_1(\kappa)$ and $\hat{f}_4(\kappa)$ are nearly identical at larger wavenumbers κ. The peaks in the real part occur near $\kappa = \pm \mathrm{Re}\, 2k_0$.

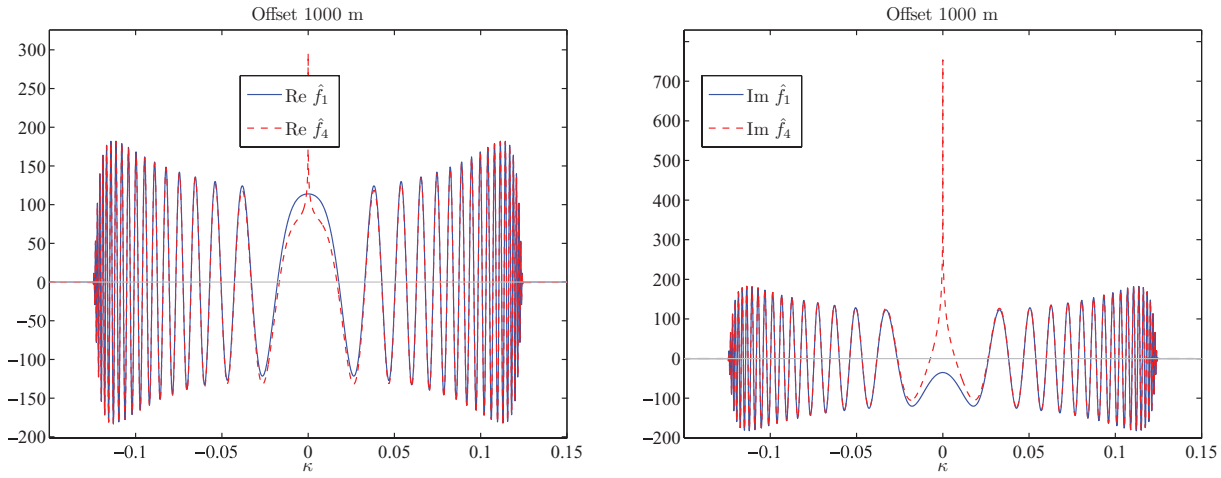

Figure 9. As Fig. 8, but for a half-offset of 1000 m. Again, the functions $\hat{f}_1(\kappa)$ and $\hat{f}_4(\kappa)$ are nearly identical at larger wavenumbers κ. The differences at small wavenumbers are substantial.

$c = (1 - w)a + wb$ and choose $w = \frac{1}{2} + \beta$. Using the properties mentioned above, we find that $||c||^2 = \frac{1}{4}||a + b||^2 + |\beta|^2||b - a||^2$, which is smallest for $\beta = 0$.

It is easy to show that the linear combination with the smallest norm, $\mu_0 = \frac{1}{2}(\mu - \mathrm{i}\mathcal{H}[\mu])$, obeys $\mu_0 = -\mathrm{i}\mathcal{H}[\mu_0]$. As we found earlier that this relation approximately holds for $m/|z_1|$, we conclude that migration of measured data provide a reconstruction of the model that approximately has this minimum-norm property.

A similar conclusion can be reached by considering the spatial Fourier transform discussed earlier in Section 3.4. If the ambiguity occurs, the recorded pressure is fairly insensitive to the positive wavenumbers of $\hat{\mu}(\kappa)$ according to eq. (7). We then can choose $\hat{\mu}(\kappa) = 0$ for $\kappa > 0$ without significantly changing the data. This implies $\hat{\mu}(\kappa) = -\mathrm{sign}(\kappa)\hat{\mu}(\kappa)$, so $\mu = -\mathrm{i}\mathcal{H}_z[\mu]$. The result is the same as the minimum-norm solution obtained by migration. The ambiguity can be removed by requiring the scattering model to be purely real-valued or purely imaginary. In the Fourier domain, a purely real-valued scattering model is obtained by setting $\hat{m}(\kappa) = \hat{m}^*(-\kappa)$ for positive κ, whereas the choice $\hat{m}(\kappa) = -\hat{m}^*(\kappa)$ leads to a purely imaginary scattering model.

4 2-D NUMERICAL EXAMPLE

So far, we have considered a simple 1-D model problem with horizontally layered scatterers in a 3-D homogeneous background and found that two different models provide nearly the same data. We wondered to what extent this conclusion holds in a more complex background model with dipped reflectors. We therefore generated synthetic data with a 2-D frequency-domain finite-difference code (Østmo *et al.* 2002; Mulder & Plessix 2004), using the Born approximation, and compared data for a given and for a transformed reflectivity model.

The transformation had to be slightly modified to account for the fact that the 2-D data represent the response of a line-source. The asymptotic result for a homogeneous model with layered scatterers is

$$\hat{p}_1^{2D}(\omega, h) \simeq \frac{(\mathrm{i} - 1)\omega^2}{8\sqrt{2\pi k_0}} \int_0^\infty \mathrm{d}z\, f_1(z)\mu(z) \frac{[1 + (h/z)^2]^{1/4}}{\sqrt{z}},$$

instead of eq. (4). For small h, this suggest depth-weighting by $\sqrt{z}$ instead of z; so, we define

$$\mathcal{M}_2[g](z) = \tilde{g}_2(z) + \tilde{g}_2(-z),$$

with

$$\tilde{g}_2(z) = -\mathrm{i}\sqrt{|z|}\mathcal{H}_z\left[g(z)\,\mathrm{sign}(z)/\sqrt{|z|}\right].$$

Fig. 10 shows the velocity and inverse quality factor for a simple salt-dome model. We smoothed the complex-valued squared slowness and obtained the perturbation ν_1 as the difference between the original and smoothed model. Fig. 11 displays the real and imaginary part of the perturbation. Fig. 12 depicts $\mathcal{M}_2[\nu_1]$, the result of applying a weighted Hilbert transform in depth and multiplication by $-\mathrm{i}$. A vertical cross-section is displayed in Fig. 13.

We computed synthetic data in both models for a shot at $x_s = 1000$ m and a depth z_s of 5 m. The receiver line had positions x_r between 1100 and 5000 m at an interval of 25 m and z_r at 5 m depth. We solved the pair of equations that represents the Born approximation of the wave equation with absorbing boundaries on all sides and transformed the frequency-domain data to the time domain with a suitable zero-phase wavelet having most of its energy between 6 and 27 Hz. Fig. 14 shows the reflection data and the difference between data for the transformed and for the original model, using the same scale. The data are clipped, and the colour scale emphasizes small amplitudes. Weak reflections generated by the absorbing boundaries and aliased in time are visible. The data agree remarkably well, as can also be seen in Fig. 15. Only the first strong sea-bottom reflection and refractions at large offsets for reflectors at shallower depths show a large difference, as do the reflections from the more strongly dipped interfaces.

We carried out a true-amplitude two-way wave-equation migration (Plessix & Mulder 2004) of a synthetic marine data set generated for the same 2-D model as before. Fig. 16 shows the real and imaginary part of the result. Fig. 17 displays a vertical cross-section of the 2-D 'true-amplitude' image at a distance of 2 km from the origin. We observe that the real and imaginary parts of the complex-valued migration result $m(x, z)$ are related by $m \simeq \mathcal{M}[m]$, as in the simple constant-velocity layered case. Discrepancies occur in the shallowest part and at depths around 1.5 km. The first is related to the strong reflections off the sea bottom, where the depth-offset ratio z/h is small. Fig. 2 shows that the approximate equality no longer holds in that case. The second discrepancy around a depth of 1.5 km is caused by the presence of the nearby steeply dipping salt flank. Apart from these two differences, the figures agree with

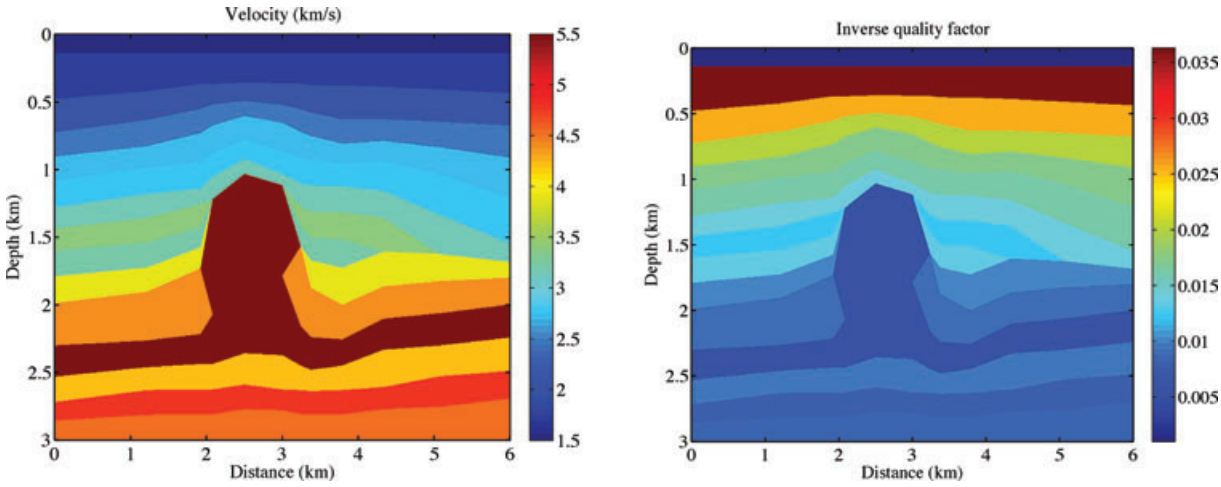

Figure 10. Original model with velocity c (left-hand panel) and inverse quality factor $1/Q$ (right-hand panel).

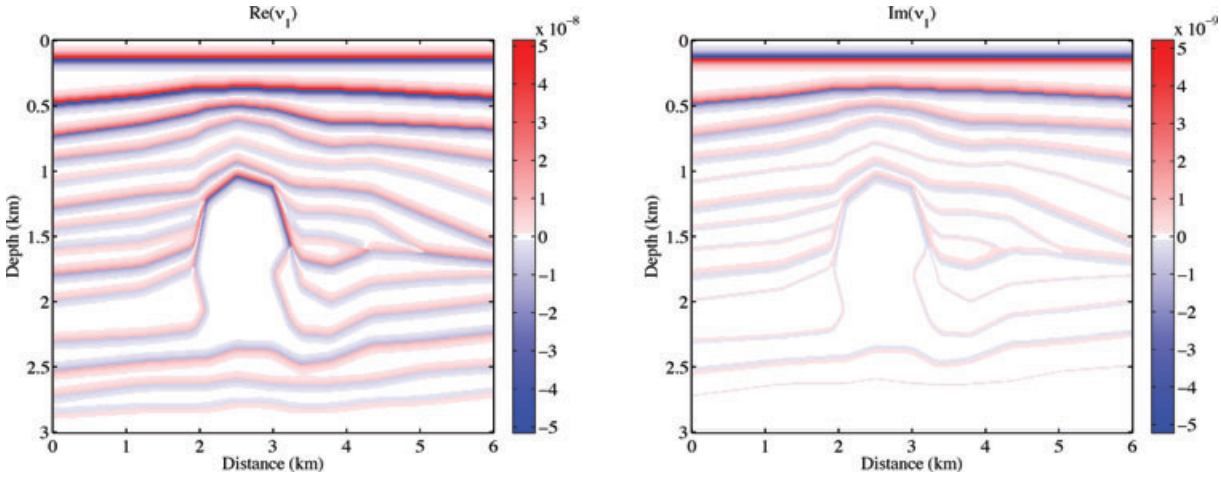

Figure 11. Real (left-hand panel) and imaginary (right-hand panel) part of the squared slowness perturbation v_1.

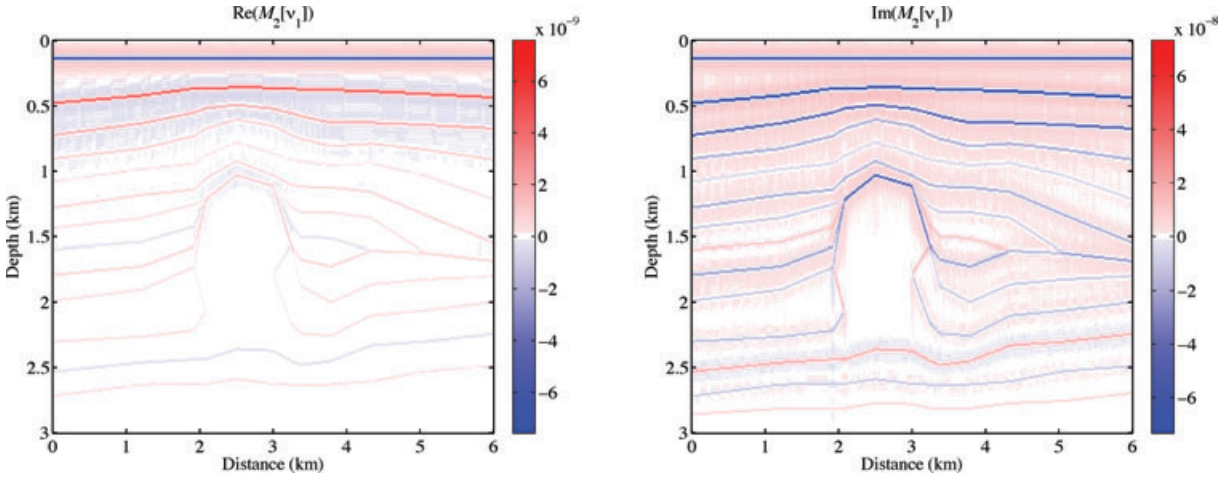

Figure 12. Real (left-hand panel) and imaginary (right-hand panel) part of of the transformed perturbations.

the fact that the migration selects the minimum-norm scattering model of the kind that was explained in Section 3.5 for horizontal reflectors. This result appears to also hold for slightly dipping reflectors.

As mentioned before, the result can be made unique by imposing constraints. If the result is assumed to be free of attenuation scattering, we can simply select the real part. If we assume that only attenuation scattering is present, we have to select the imaginary

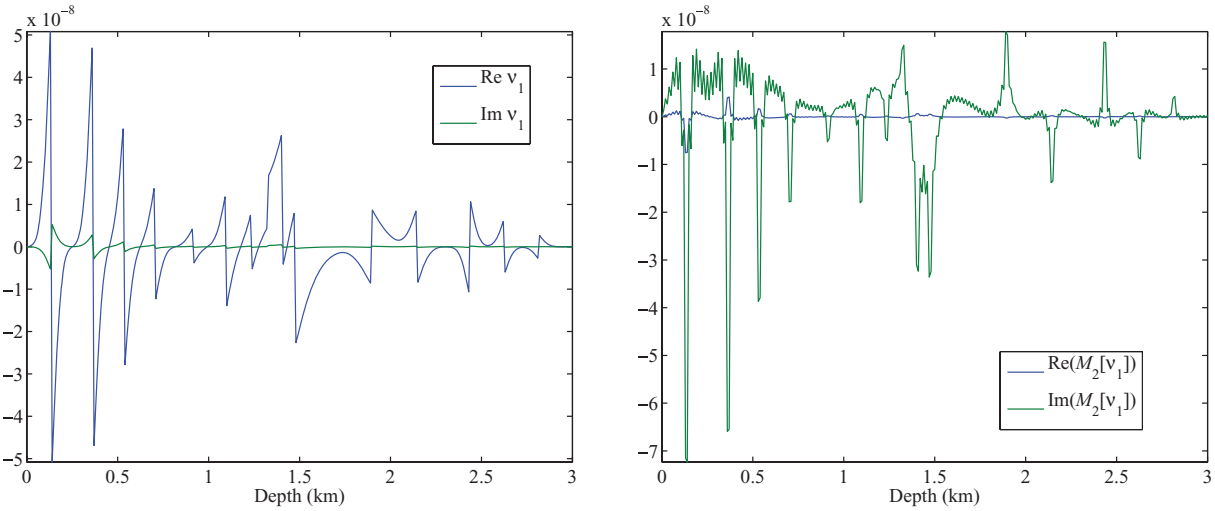

Figure 13. Cross-sections at 2 km distance from the origin. The left-hand panel shows the real (blue) and imaginary (green) part of the scatterers, the right-hand panel shows the scatterers after the depth-weighted Hilbert transform.

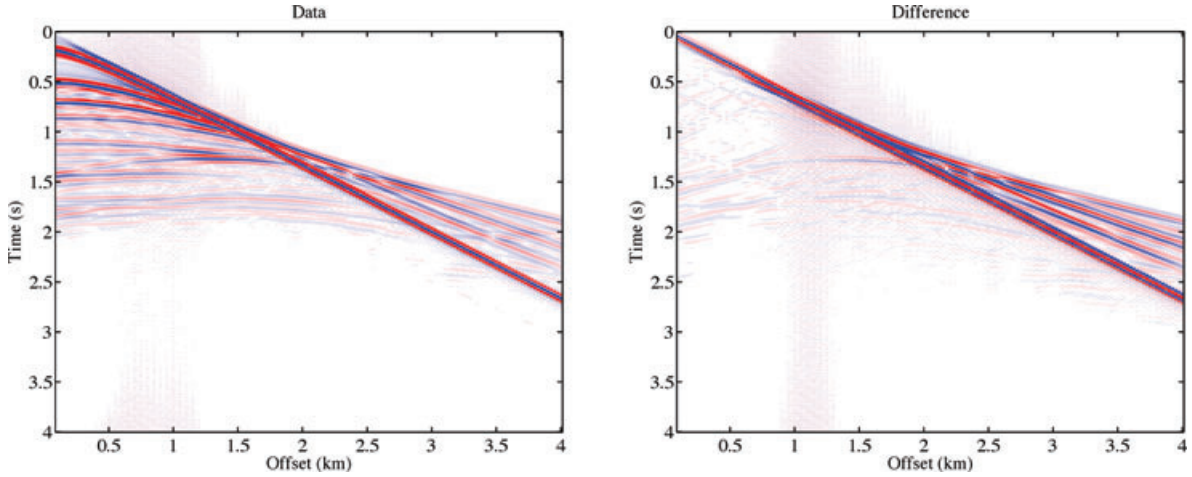

Figure 14. The data (left-hand panel) and the difference (right-hand panel) between data generated in the transformed and in the original model, both with the same scale. We applied a clip at 5 per cent of the maximum absolute value of the data in the left-hand panel.

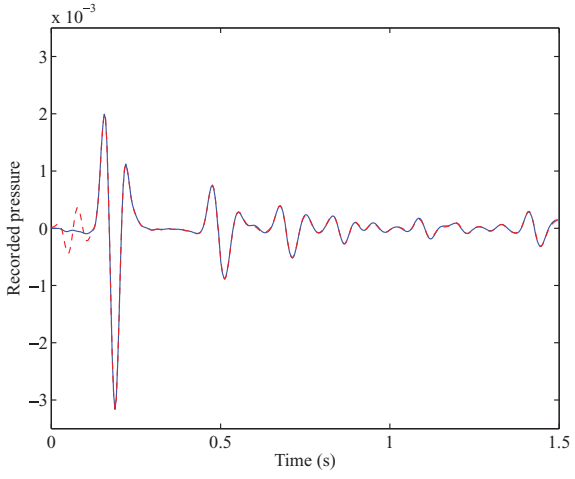

Figure 15. Single trace at 100 m offset. The blue line represents the data for original model, the red dashed line for the transformed one.

part. Without such constraints, inverting for both at the same time in a linearized sense will be problematic.

5 DISCUSSION

We have shown that two different scattering models provide almost identical data. This implies that it, in practice, it will be impossible to uniquely determine both the velocity and attenuation perturbations from the data, unless with additional constraints. The transformed model, for instance, when added to the background model, corresponds to unphysical values of the perturbed attenuation, both in size and sign. Suitable constraints on the admissible solution will reduce, but possibly not remove, the ambiguity. Requiring the result to be without attenuation will remove the ambiguity, as will the constraint that the scattering is caused by attenuation perturbations only.

Our result seems to contradict conclusions on visco-acoustic inversion by several authors, including ourselves; so, some comments are in place.

The existence of non-radiating sources (Bohm & Weinstein 1948; Goedecke 1964; Bleistein & Cohen 1977; Devaney 1978; Devaney

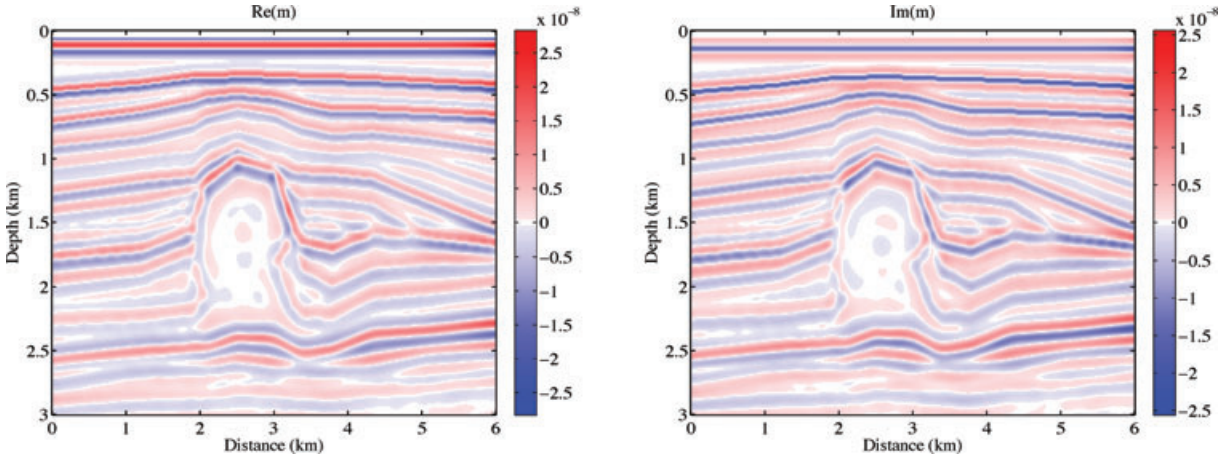

Figure 16. Real (left-hand panel) and imaginary part (right-hand panel) of the migration result.

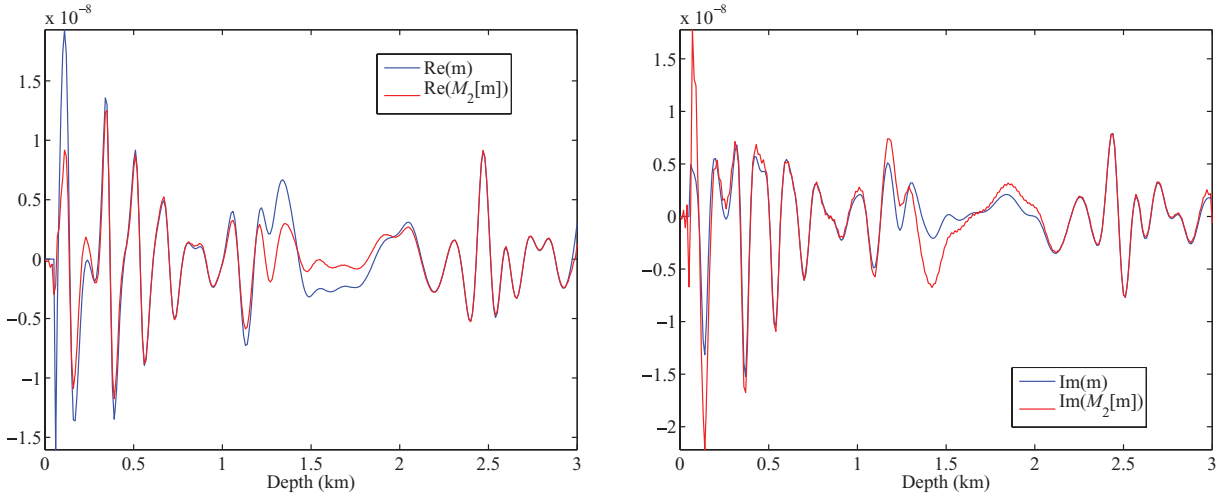

Figure 17. Cross-sections of the migration image at 2 km distance from the origin. The blue line represents the result for the original model, the red line for the transformed one. The real part is shown in the left-hand panel, the imaginary part in the right-hand panel.

& Marengo 1998) can be related the non-uniqueness in scattering by noting that the product of the incoming wavefield with the the scatterer potential acts as a secondary source (Devaney & Sherman 1982; Hoenders 1997; Devaney 2004). According to Devaney & Sherman (1982), the non-uniqueness in scattering should disappear if multiple experiments are performed, for instance, at more than a single offset.

Ribodetti *et al.* (1995) and Hak & Mulder (2008) consider delta-function type perturbations or point scatterers. Its Fourier transform in depth contains long-wavelength components, including the zero wavelength. As demonstrated in Section 3.4, the ambiguity disappears for small wavenumbers that correspond to long wavelengths and linearized inversion should therefore be feasible. For scatterers that resemble the first or higher derivative in z of a delta-function or Gaussian with small width, the long-wavelength components are small and the ambiguity should appear. This happens in the 2-D example presented here. The sea bottom is an exception, as are shallow refractions at large offsets and reflections off dipping interfaces.

Ribodetti *et al.* (1995) demonstrated that density, velocity, and attenuation perturbations can be recovered by inversion, but they only consider perturbations in one of these parameters at a time. With the constraint that the inverted parameter is either real or imaginary, the ambiguity is removed. Similarly, Blanch & Symes (1994) only consider a perturbation of the bulk modulus or bulk modulus and density (Blanch & Symes 1995) in a visco-acoustic background model.

Ribodetti & Virieux (1998) presented linearized inversion results for scattering by blocky models. The Hilbert transform of a square wave has logarithmic singularities at positions corresponding to the ramps of the square wave. Such singularities should be visible as large peaks. Indeed, the reconstructed attenuation profiles in the paper by Ribodetti & Virieux (1998) sometimes show peaks at the jumps, rather than the under- and overshoots next to these jumps, which are typical for least-squares inversion of blocky models in the real-valued case. Also, Innanen & Weglein (2007) consider blocky models that contain long spatial wavelengths, and can invert for the scattering model parameters.

We should emphasize that our observations do not relate to attenuation estimates from diving waves or direct arrivals in crosswell or VSP transmission data. These provide a characterization of the background model.

6 CONCLUSION

We have demonstrated that different scattering models provide almost the same data if attenuation scattering is included. The

ambiguity occurs for scatterers with small dip that are located sufficiently deep and that have an oscillatory character. The last condition is typically met when migrating seismic data. Because the data are band-limited, the migration algorithm will only be able to reconstruct the difference between a rough earth model and its smoothed version. This difference is oscillatory by definition. As a consequence, attenuation scattering imaging will be nearly impossible without imposing additional constraints. The ambiguity can be removed by requiring the scatterer to have no attenuation at all or to be purely attenuative.

ACKNOWLEDGMENTS

This work is part of the research programme of the 'Stichting voor Fundamenteel Onderzoek der Materie (FOM)', financially supported by the 'Nederlandse Organisatie voor Wetenschappelijk Onderzoek (NWO)' and by 'Stichting Shell Research'.

REFERENCES

Aki, K. & Richards, P.G., 1980. *Quantitative Seismology: Theory and Methods,* Vol. 1, W.H. Freeman and Company, San Francisco.

Beylkin, G., 1985. Imaging of discontinuities in the inverse scattering problem by inversion of a causal generalized Radon transform, *J. Math. Phys.,* **26**(1), 99–108.

Blanch, J.O. & Symes, W.W., 1994. Linear inversion in layered viscoacoustic media using a time-domain method, *SEG Tech. Prog. Expanded Abstracts,* **13,** 1053–1056.

Blanch, J.O. & Symes, W.W., 1995. Efficient iterative viscoacoustic linearized inversion, *SEG Tech. Prog. Expanded Abstracts,* **14,** 627–630.

Bleistein, N. & Cohen, J.K., 1977. Nonuniqueness in the inverse source problem in acoustics and electromagnetics, *J. Math. Phys.,* **18**(2), 194–201.

Bohm, D. & Weinstein, M., 1948. The self-oscillations of a charged particle, *Phys. Rev.,* **14**(12), 1789–1798.

Chavent, G. & Plessix, R.-É., 1999. An optimal true-amplitude least-squares prestack depth-migration operator, *Geophysics,* **64**(2), 508–515.

Devaney, A.J., 1978. Nonuniqueness in the inverse scattering problem, *J. Math. Phys.,* **19**(7), 1526–1531.

Devaney, A.J., 2004. Nonradiating surface sources, *J. Opt. Soc. Am. A,* **21**(11), 2216–2222.

Devaney, A.J. & Marengo, E.A., 1998. A method for specifying nonradiating, monochromatic, scalar sources and their fields, *J. Opt. A (Pure and Applied Optics),* **7**(5), 1213–1220.

Devaney, A.J. & Sherman, G.C., 1982. Nonuniqueness in inverse source and scattering problems, *IEEE Trans. Antennas Propagat.,* **30**(5), 1034–1037.

Docherty, P., 1991. A brief comparison of some Kirchhoff integral formula for migration and inversion, *Geophysics,* **56**(8), 1164–1169.

Goedecke, G.H., 1964. Classically radiationless motions and possible implications for quantum theory, *Phys. Rev.,* **135**(1B), 281–288.

Gradshteyn, I.S. & Ryzhik, I.M., 1965. *Table of Integrals, Series, and Products,* 4th edn, Academic Press, New York.

Gray, S., 1997. True amplitude migration: a comparison of three approaches, *Geophysics,* **62**(3), 929–936.

Hak, B. & Mulder, W.A., 2008. Preconditioning for linearised inversion of attenuation and velocity perturbations, in *Proceedings of the 70th EAGE Conference & Exhibition incorporating SPE EUROPEC (Extended Abstracts)*, European Association of Geoscientists & Engineers, EAGE, Houten, p. H002.

Hoenders, B.J., 1997. Existence of invisible nonscattering objects and nonradiating sources, *J. Opt. Soc. Am. A,* **14**(1), 262–266.

Innanen, K.A. & Weglein, A.B., 2007. On the construction of an absorptive-dispersive medium model via direct linear inversion of reflected seismic primaries, *Inverse Problems,* **23**(6), 2289–2310.

Mulder, W.A. & Plessix, R.-É., 2004. A comparison between one-way and two-way wave-equation migration, *Geophysics,* **69**(6), 1491–1504.

Østmo, S., Mulder, W.A. & Plessix, R.-É., 2002. Finite-difference iterative migration by linearized waveform inversion in the frequency domain, *SEG Tech. Prog. Expanded Abstracts,* **21,** 1384–1387.

Plessix, R.-É. & Mulder, W.A., 2004. Frequency-domain finite-difference amplitude-preserving migration, *Geophys. J. Int.,* **157**(3), 975–987.

Ribodetti, A. & Virieux, J., 1998. Asymptotic theory for imaging the attenuation factor *Q, Geophysics,* **63**(5), 1767–1778.

Ribodetti, A., Virieux, J. & Durand, S., 1995. Asymptotic theory for viscoacoustic seismic imaging, *SEG Tech. Prog. Expanded Abstracts,* **14,** 631–634.

Shin, C., Jang, S. & Min, D.J., 2001. Improved amplitude preservation for prestack depth migration by inverse scattering theory, *Geophys. Prospect.,* **49**(5), 592–606.

Sirgue, L. & Pratt, R.G., 2004. Efficient waveform inversion and imaging: a strategy for selecting temporal frequencies, *Geophysics,* **69**(1), 231–248.

ten Kroode, A.P.E., Smit, D.J. & Verdel, A.R., 1994. A microlocal analysis of migration, *Wave Motion,* **28**(2), 149–172.